Journal of Energy Storage 109 (2025) 115182

Contents lists available at ScienceDirect

Journal of Energy Storage

journal homepage: www.elsevier.com/locate/est

Research Papers

Manganese-doped iron sulfide nanoplatelets on carbon cloth: A negative electrode material for flexible and wearable supercapacitors

Almila Nur Gözütok [a,1], Mete Batuhan Durukan [b,1], Yusuf Kocak [c], Emrah Ozensoy [c,d], Husnu Emrah Unalan [b,*], Emren Nalbant [a]

[a] Department of Chemistry, Middle East Technical University (METU), Ankara 06800, Türkiye
[b] Department of Metallurgical and Materials Engineering, Middle East Technical University (METU), Ankara 06800, Türkiye
[c] Chemistry Department, Bilkent University, 06800 Ankara, Türkiye
[d] UNAM-National Nanotechnology Center, Bilkent University, 06800 Ankara, Türkiye

ARTICLE INFO

Keywords:
Wearable supercapacitors
Bimetallic sulfides
Flexible supercapacitors
Gel electrolyte
Negative electrode

ABSTRACT

Herein, we report the direct growth of manganese-doped iron sulfide (pyrrhotite) nanoplatelets on the carbon cloth (CC) fibers by a one-step hydrothermal method without the need for organic binders. Manganese-doped iron sulfide nanoplatelets on CC (MFS-CC) revealed surface enrichment of polysulfide species over sulfites, exhibited a variety of $Mn^{2+/3+/4+}$, $Fe^{3+/4+}$ surface species as well as unique $Fe_xMn_yO_zS_n$ surface domains resulting in a multitude of electroactive sites, enhancing ion transport and an exceptional electrochemical performance. As-prepared electrodes yielded a high specific capacitance of 206 F g^{-1} at a scan rate of 10 mVs^{-1}. Moreover, once constructed, the electrodes were encapsulated with polyvinyl chloride (PVC) to ensure efficient operation for up to three months. As a result, the device demonstrated remarkable cyclic stability, enduring up to 11,000 cycles without degradation. Finally, the assembled electrodes were integrated to form an asymmetric wearable supercapacitor, and this device effectively illuminated a green light emitting diode (LED) integrated into a hoodie, showcasing its potential for powering wearable electronics.

1. Introduction

Supercapacitors become an intriguing energy storage alternative to batteries due to their high-power density and fast charging capabilities. Supercapacitors' potential is further amplified as potential energy storage devices for flexible and wearable devices. Lately, a growing emphasis has been on investigating flexible and wearable supercapacitors. They are transforming the landscape of lightweight, portable energy storage systems, enabling the creation of smart textiles and powering an array of applications spanning from health monitoring devices to smart clothing and beyond. This is further supported by the ability to form supercapacitor materials on carbon cloths (CCs) to integrate wearable supercapacitors with wearable electronic devices seamlessly. In recent years, curiosity has been piqued by rapidly developing wearable electronics, such as bio-monitoring gadgets, military gear, electrical sensors, wristwatches, eyeglass technologies, and displays [1–4]. Flexible supercapacitors have begun to be utilized extensively as a power supply for wearable electronics because of their high-power densities, long lifespans, fast charging/discharging capabilities, availability, and safety, in addition to lower cost and safe operation advantage over Li-ion battery technologies [4–6]. However, low energy density fundamentally limits the range of applications of supercapacitors in industry [7]. To meet higher standards of the energy density of future wearable devices, transition metal sulfides/oxides have been extensively researched as potential electrode materials for asymmetric supercapacitors (ASCs) [8–10].

Bimetallic sulfides/oxides are now the material of choice due to the synergistic effect of two metal ions, which facilitates the faradaic redox process and enhances the electrochemical performance of supercapacitors. Additionally, they are attractive as electrode materials because of their high specific charge capacity, numerous valence states, conductivity, and low cost [11–13]. In recent years, research efforts have also focused on alternative transition metal-based materials, mainly transition metal oxides with high specific capacitance values. They have been comprehensively analyzed in many studies and reviews [14–21]. However, with the introduction of bimetallic sulfides, notable

* Corresponding author.
E-mail address: unalan@metu.edu.tr (H.E. Unalan).
[1] Equal contribution.

https://doi.org/10.1016/j.est.2024.115182
Received 12 June 2024; Received in revised form 28 November 2024; Accepted 22 December 2024
Available online 31 December 2024

advancements in electrochemical activities have been achieved due to the smaller electronegativity of the sulfur atoms in the metal sulfides as opposed to oxide ions in metal oxide architectures, facilitating electron transfer processes in the former case [9,22].

Amidst bimetallic sulfides, nickel cobalt sulfide ($NiCo_2S_4$) has been investigated by Shen et al., and a specific capacitance of 877 F g^{-1} was reported at a current density of 20 A g^{-1} [23]. Zhang et al. fabricated flower-like copper cobalt sulfide ($CuCo_2S_4$) by hydrothermal method, accomplishing 908 F g^{-1} at 30 mA cm^{-2} [24]. Among various bimetallic sulfides, manganese cobalt sulfide ($MnCo_2S_4$) [25], iron-cobalt sulfide ($FeCo_2S_4$) [26], and copper iron sulfide ($CuFe_2S_2$) [13] have also been investigated, and promising results have been reported. Additionally, Li et al. prepared manganese-iron sulfide ($Mn_{0.6}Fe_{0.4}S$) for application in Li-ion batteries, showcasing a capacity of 520 mAh g^{-1} at a current density of 1 A g^{-1} [27]. Although manganese (Mn) and iron (Fe) are promising materials in promoting redox processes due to their multiple valence states, affordability, and abundance compared to other transition metals, there has been a lack of research on the use of manganese-iron-sulfur-based electrode materials, especially in the field of wearable supercapacitors. Besides, since the currently available bimetallic negative electrode structures that can be utilized for supercapacitor applications are limited, and conventional negative electrodes still suffer from low conductivity, further studies are required to fulfill the requisites of future energy storage applications.

Synthesizing stable nanoscale iron sulfides poses inherent challenges due to the strong tendency of ferric ions to react with oxygen, potentially resulting in the formation of iron oxides during the synthetic processes [28]. Herein, we successfully demonstrate the synthesis of manganese-doped iron sulfide (pyrrhotite – named hereon as MFS) directly on CC, which yielded a binder-free, highly conductive, wearable, and flexible material as a potential negative electrode. The exceptional structure of the currently synthesized MFS-based negative electrode revealed surface enrichment of polysulfide species over sulfites, exhibited a variety of $Mn^{2+/3+/4+}$, $Fe^{3+/4+}$ surface species and unique $Fe_xMn_yO_zS_n$ surface domains resulting in enhanced electrochemical performance. Furthermore, the straightforward hydrothermal method was chosen since it promotes the coupling of the active material with the entire 3D network of the textile, resulting in a significant surface area and eliminating the need for non-conductive binders by direct growth [13,29–31]. Also, we constructed a flexible and wearable device employing an exceptional encapsulation method, demonstrating remarkable performance after 3 months of production. These findings contribute to the growing research on utilizing manganese-iron-sulfur-based negative electrode materials for advanced energy storage applications.

2. Experimental section

2.1. Fabrication of oxygen plasma-modified CC electrodes

Prior to the hydrothermal process, CC (hydrophobic carbon cloth, W1S1011, Carbon Energy, China) was sonicated in acetone, ethanol, and deionized water (DIW) for 15 min each and then dried. Oxygen-plasma treatment was applied on CC via a Femto Science Cute Plasma System for 5 min, and CCs were then used without further modification.

2.2. Direct growth of MFS, MS, and FS on CC

All chemicals were used as received without further purification. MFS nanoplatelets were decorated on CC by a one-pot hydrothermal approach. First, 5 mmol iron (II) chloride tetrahydrate ($FeCl_2.4H_2O$, ≥ 99.0, Sigma-Aldrich), 5 mmol manganese (II) chloride tetrahydrate ($MnCl_2.4H_2O$, ≥ 99.0, Sigma-Aldrich), and 10 mmol thioacetamide (TAA, C_2H_5NS, Supelco) were dissolved in 30 mL isopropanol (IPA) and 10 mL DIW. The solution was stirred vigorously at room temperature until complete dissolution. Afterward, the prepared solution was transferred into a Teflon-lined stainless steel autoclave with the oxygen plasma-modified CC. It was kept at 120 °C for 48 h to obtain MFS nanoplatelets on CC, washed with DIW, and named MFS-CC. The same procedure was applied to prepare MnS and FeS on CC. The resulting materials were called MS-CC and FS-CC. The mass loadings of MFS-CC and MS-CC were 1.12 mg/cm^2 and 1.7 mg/cm^2, respectively. The obtained powders were centrifuged and washed with DIW and ethanol, followed by drying in an oven overnight at 80 °C for further characterization.

2.3. Materials characterization

Scanning electron microscopy (SEM) and energy-dispersive X-ray (EDX) mapping were carried out via an FEI QUANTA 400F Field Emission SEM. Transmission electron microscope (TEM) images and additional EDX spectra were acquired at an acceleration voltage of 300 kV using a Jeol JEM 2100F TEM system equipped with an EDX setup. A Rigaku D/Max-2000 X-ray diffractometer with Cu Kα radiation at a scanning rate of 1°/min was employed to carry out X-ray diffraction (XRD) analysis. X-ray photoelectron spectroscopy (XPS) experiments were carried out with a SPECS HSA3500 hemispherical energy analyzer and a PHOIBOS 100 detector with an MCD-5. During the XPS data acquisition, a monochromatic Al-Kα X-ray excitation source (14 kV, 350 W, 1486.6 eV) was employed, along with an electron flood gun for charge compensation. The pass energy value used in the high-resolution core level XPS spectra was 20 eV. Binding energy (B.E.) values of the XP spectra were shifted to the C1s line of the adventitious carbon at 284.6 eV. XPS data analysis was conducted via the CasaXPS software, and background subtraction was performed using a Shirley background. Peak positions and peak areas were estimated via a weighted least-squares fitting method using 70 % Gaussian and 30 % Lorentzian peak line shapes. Surface elemental quantification was performed by employing Scofield's relative sensitivity factors.

2.4. Electrochemical measurements

All electrochemical measurements were conducted in typical three electrode and full cell systems using a Biologic VMP3 Potentiostat/Galvanostat setup. MFS-CC, saturated calomel electrode, and platinum sheet were used as working, reference, and counter electrodes, respectively. All the measurements were made using 1.0 M potassium hydroxide ($KOH_{(aq)}$) electrolyte solution. For the fabrication of the flexible devices and full cell measurements, carbon black (CB – Alfa Aesar, Acetylene Black 50 % compressed, 99.9 + %)/activated carbon (AC – Alfa Aesar Carbon, activated, −20 + 40 mesh) mixture, *N*-methyl-2-pyrrolidone (NMP – Thermo Scientific Chemicals, ACS grade, 99.0 + %), and polyvinylidene fluoride (PVDF – Sigma Aldrich, $M_w \approx 180{,}000$) were used at a ratio of 80:15:5 and sonicated for 45 min to prepare positive electrode. The obtained slurry was applied to the CC (1 × 2 cm^2) with a brush and kept overnight at 100 °C in a vacuum oven, later given the name AC-CC. The active material loading was determined by measuring the weight change upon slurry application. A gel electrolyte based on cellulose was prepared by heating a combination of 4 g of 2-Hydroxyethyl cellulose (HEC - Sigma-Aldrich, $M_w \approx 90{,}000$) and 60 mL of deionized water until a transparent solution was obtained. At least 2 h of stirring is practiced to obtain a clear gel. Once the gel cleared, 6 g of 10.0 M $KOH_{(aq)}$ was added dropwise, and the mixture was cooled to room temperature. After adding and stirring 0.2 g of glycerol, a disposable non-woven cloth was coated with a thin gel electrolyte layer and used as a separator. The electrodes were sealed with polyvinyl chloride (PVC) lamination, and untreated hydrophobic CC was used for the contacts. The designated device was named MFS-CC//AC-CC.

3. Results and discussion

A schematic illustration of the preparation process for the MFS-CC is provided in Fig. 1a. MFS nanoplatelets were directly grown on the fibers

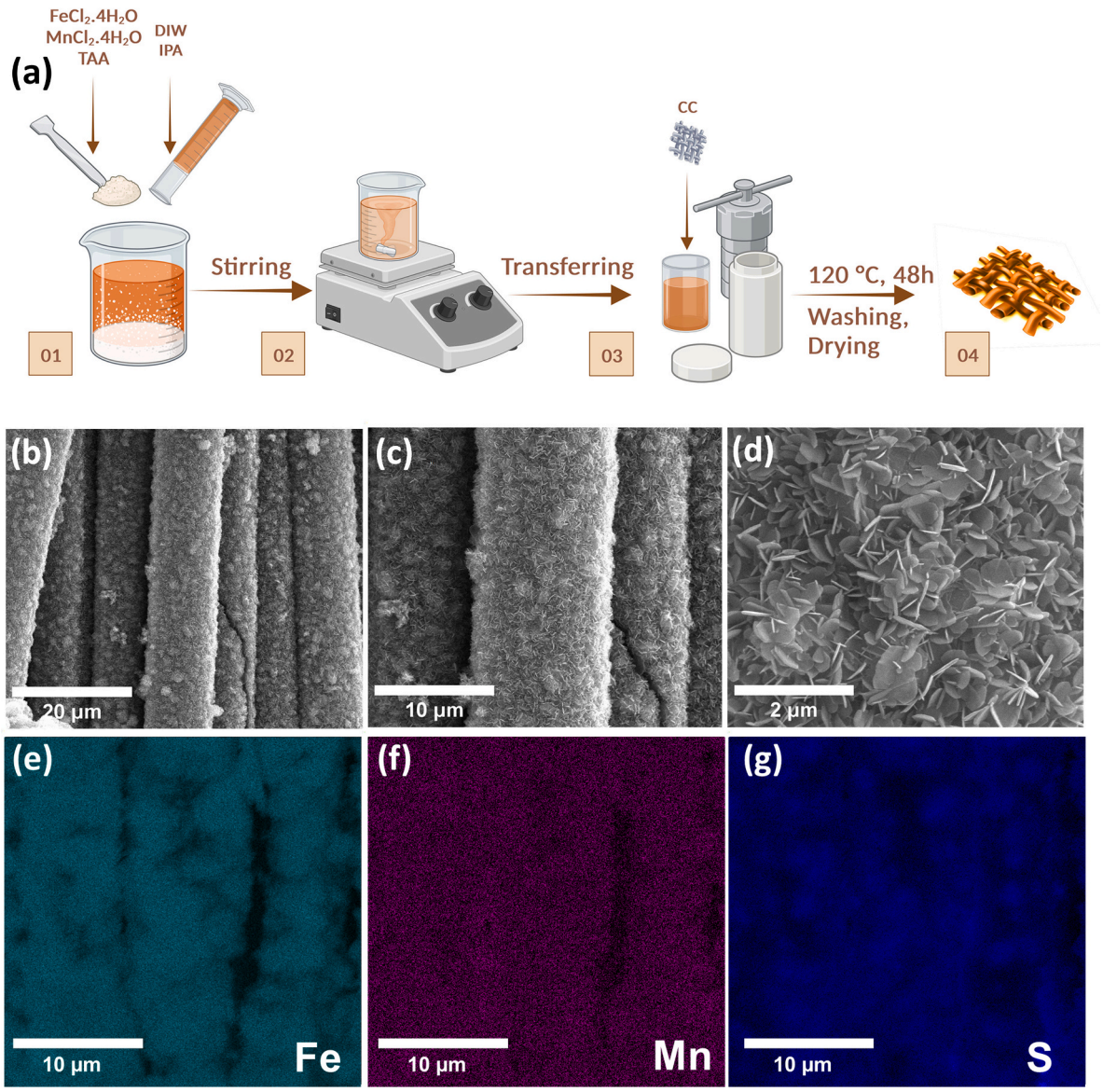

Fig. 1. (a) Schematic illustration of the growth procedure, (b–d) SEM images of the MFS-CC from low magnification to high magnification, (e) Fe, (f) Mn, and (g) S EDX-maps of MFS-CC.

of the CC using the hydrothermal method. CC cloths were subjected to oxygen plasma to make them hydrophilic prior to the hydrothermal reaction. This ensures the wetting of the reaction solution on the CC, ensuring the growth directly on the fibers. Relevant photos of the wetting difference are given in Fig. S1. The same procedure was also conducted to prepare manganese sulfide on CC without adding an iron precursor named manganese sulfide on carbon cloth (MS-CC) (detailed information can be found in the experimental section).

The morphology of the prepared MFS-CC was examined via SEM. Fig. 1b–d shows SEM images of the nanoplatelets grown on the CC acquired with various magnifications. Oxygen-plasma treatment on CC led to a hydrophilic surface, thereby facilitating a relatively even coating of MFS across the fibers of the cloth. In the low-magnification SEM images (Fig. 1b–c), it can be seen that MFS nanoplatelets are more homogeneously decorated onto the fibers of the CC compared to MS nanoplatelets on MS-CC. It can also be observed that the growth on FS-CC, without the presence of Mn, is incomplete and not homogeneous (Fig. S2). This also indicates that the conformal growth on CC necessitates introducing Mn to the FS-CC. This also indicates uniform and homogeneous growth on CC allowed by the introduction of Mn to the system. From this point on, we discontinued the fabrication of FS-CC due to our inability to achieve conformal growth on CC. The high-magnification image in Fig. 1d illustrates the 2D flake-like nanoplatelet morphology of the MFS overlayer on the CC surface, where the MFS nanoplatelets reveal a typical diameter of ca. 500 nm and a thickness of ca. 80 nm. Such homogeneously-packed nanoplatelet overlayers have been reported to aid ion migration into electrode materials and provide abundant electroactive sites for energy storage [32]. EDX maps of the synthesized materials (Fig. 1e–g) verified the existence of Fe, Mn, and S along the fibers of the carbon cloth. The EDX spectrum and elemental maps of the Cl and O are given in Fig. S3a–c. Remnant Cl from the reactants is visible in the spectrum. We believe that the Cl was mainly latched onto the CC, and gentle cleaning of the MFS-CC was insufficient to remove the remnants. The presence of the O was due to the partial surface oxidation of MFS's, and well expected due to the nature of the hydrothermal reaction.

TEM analysis was conducted to examine the structure of the MFS powder further, and the resulting images are given in Fig. 2a. MFS particles grown on CC can be observed in Fig. 2a-i. Confirming the SEM images, Fig. 2a-ii clearly shows the structure's sharp hexagonal edges.

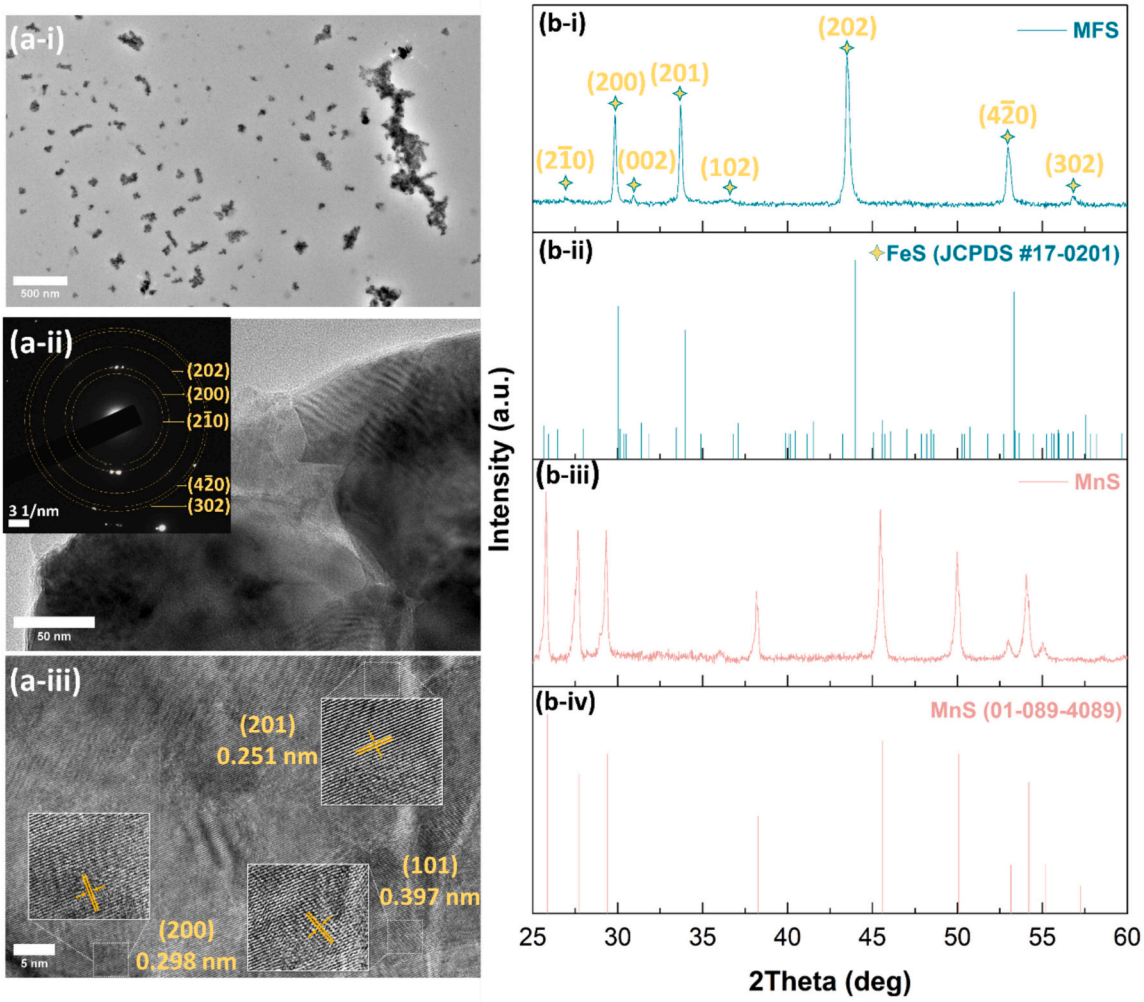

Fig. 2. (a) TEM images of the MFS nanoplatelets with (i, ii, iii) different magnifications. Inset in (a-ii) shows the corresponding SAED pattern and corresponding (hkl) planes. (a-iii) shows the (b) XRD patterns of (b-i, b-iii) the as-synthesized materials with (b-ii) hexagonal pyrrhotite structure and (b-iv) hexagonal wurtzite structure.

The selected area diffraction pattern (SAED) indicates the preferential orientation of the synthesized material (inset in Fig. 2a-ii). Planes detected in the SAED pattern are provided in this inset. Diffractions from (2$\bar{1}$0), (200), (202), (4$\bar{2}$0), and (302) can be detected. Analysis of high-resolution TEM (HRTEM) image in Fig. 2a-iii revealed the d-spacing values of 0.397, 0.298, and 0.251 nm corresponding to (101), (200), and (201) planes, respectively. The TEM-EDX spectrum in Fig. S4 further demonstrates the presence of the iron, sulfur, and manganese elements in the structure.

XRD patterns for MFS and MS powders are provided in Fig. 2b. Well-defined diffraction peaks indicate the crystalline character for both MFS and MS materials matching well with hexagonal pyrrhotite (FeS) structure (JCPDS card no. 17–0201) and hexagonal wurtzite MnS structure (JCPDS card no. 01–089-4090), respectively. Notably, the XRD pattern of the MFS sample reveals a strong match with the hexagonal pyrrhotite structure with the $P6_3mc$ space group, with no trace of an impurity phase. This shows that the addition of Mn helps stabilize the pyrrhotite structure. Significantly, the XRD peak locations in the MFS nanoplatelets display a slight shift towards lower degrees, indicating the successful incorporation of Mn cations into the pyrrhotite host matrix. This shift occurs owing to increased space between crystal planes caused by the greater atomic radius of the dopant Mn than Fe, contributing to a reduction in the diffraction angle in line with the Bragg equation. Crucially, the absence of MnS peaks in the XRD pattern of MFS strongly suggests that Mn atoms have been successfully integrated into the FeS lattice rather than producing separate FeS and MnS domains [33].

The surface chemistry of MFS and MnS negative electrodes was examined in detail via XPS analysis (Fig. 3a–g). XPS survey spectra (Fig. S5) verified the presence of Fe, Mn, S, C, O, N, and Cl in all samples. It is likely that the C1s signal in XPS originates from TAA used in the synthesis and adventitious carbon (Figs. S6a, Fig. 3a), while Cl2s and Cl2p signals in XPS (Figs. S5) stem from metal chloride precursors used in the synthesis. N1s signal in XPS (Fig. S5) is also due to residual TAA used in the synthesis. The presence of a readily visible O1s signal in XPS (Figs. S6b) can be ascribed to the partial oxidation of the samples upon exposure to air. As will be discussed below, presumably some of these oxygen species are associated with the oxidation of polysulfides (S_n^{2-}) forming sulfite (SO_3^{2-}) species (particularly in the case of MnS), as well as substitution of sulfide species with O^{2-} species (particularly in the case of MFS).

Surface atom concentration values determined from XPS data are presented in Fig. 3a. It is apparent that the ratio of the sulfur atoms to the total number of metal atoms (i.e., S/M) on the surface is higher for MFS (S/M = 0.41) as compared to that of MnS (S/M = 0.37) suggesting the enrichment of sulfur species on the MFS sample. Furthermore, surface metal cation sites of the MFS sample are dominated by Fe species rather than Mn, evident by the Fe:Mn surface atom ratio of 0.7:0.3. This observation is in very good agreement with the current XRD data (Fig. 2), suggesting that the bulk crystal structure of the MFS system is predominantly comprised of hexagonal pyrrhotite (FeS) doped with Mn.

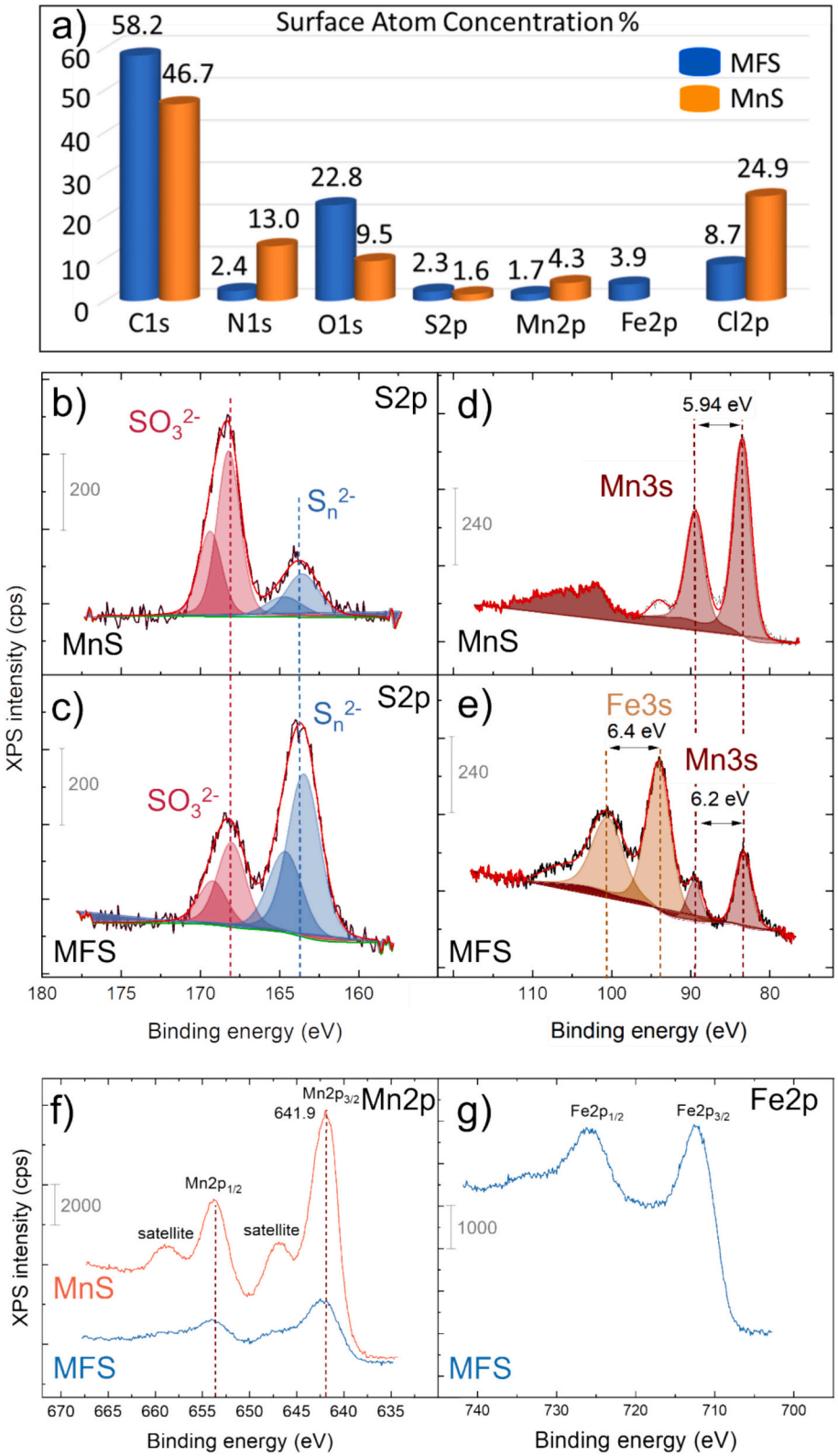

Fig. 3. (a) Surface atom concentration (%) values of MnS and MFS obtained from XPS data. (b-c) S2p, (d-e) Mn3s, (f) Mn2p XPS data for MnS and MFS. (g) Fe2p XPS data for MFS.

Fig. 3a also reveals that MnS sample contains noticeably higher amounts of surface N and Cl atoms (13.0 % and 24.9 %) than that of MFS (2.4 % and 8.7 %) indicating that the MnS sample surface contains substantially higher levels of unreacted TAA and $MnCl_2$ residues, respectively. Furthermore, a significantly higher amount of surface O species (22.8 %) on MFS as opposed to MnS (9.5 %) is detected despite a relatively smaller extent of oxidized sulfur species (i.e., SO_3^{2-}) on MFS (Fig. 3b–c). This suggests that sulfides in the MFS structure are more prone to substitution with O^{2-} species upon oxidation and exposure to air.

S2p XPS data for MnS and MFS (Fig. 3b–c) yield two broad features

corresponding to two different types of sulfur species, namely polysulfides (S_n^{2-}) and sulfites (SO_3^{2-}) [34,35]. Note that due to the small spin-orbit splitting of S2p signals, each of these broad signals given in Fig. 3b–c are comprised of two intrinsic peaks (i.e., a more intense $S2p_{3/2}$ signal appearing at a lower B.E. and a less intense $S2p_{1/2}$ signal appearing at a higher B.E. value at same colors). Accordingly, S2p XPS spectrum of the MnS sample (Fig. 3b) reveals polysulfide features located at 163.5 ($S2p_{3/2}$) and 164.7 eV ($S2p_{1/2}$), as well as sulfite features located at 168.2 ($S2p_{3/2}$) and 169.3 eV ($S2p_{1/2}$), respectively. Similar S2p features are also visible for the MFS sample (Fig. 3c) at 163.4 eV (S_n^{2-}, $S2p_{3/2}$), 164.6 eV (S_n^{2-}, $S2p_{1/2}$), 168.0 eV (SO_3^{2-}, $S2p_{3/2}$), and 169.2 eV (SO_3^{2-}, $S2p_{1/2}$). It is worth mentioning that enrichment of the MFS surface with polysulfide species and immobilization of S_n^{2-} species on the negative electrode surface can favor electrochemical performance. It was recently reported that polysulfide species bound to the electrode surface might limit the polysulfide diffusion, suppress the polysulfide dissolution, and thus enhance the charge transfer rate and boost the electrochemical performance [36].

Mn3s XPS spectra can be used to estimate the average oxidation state (AOS) of Mn species. Galakhov et al. [37] demonstrated that Mn3s splitting energies (i.e., Δ) varied rather linearly as a function of Mn AOS via the following relationship: AOS = 8.95–1.13Δ. Fig. 3d–e illustrates that Mn3s splitting values for MnS and MFS are 5.9 and 6.2 eV, corresponding to Mn AOS values of +1.95 and + 2.30, respectively. This observation is in accordance with the previously discussed current findings suggesting that Mn sites of MFS are more prone to oxidation than that of MnS and the sulfide species in the MFS structure can be more readily substituted with O^{2-} species. In other words, it is apparent that while MnS structure almost exclusively contains Mn^{2+} cations, MFS structure includes predominantly Mn^{2+} cations with a lesser but noticeable contribution from $Mn^{3+/4+}$ sites. Prominent presence of Mn^{2+} states on MnS and MFS surfaces are also supported by the corresponding Mn2p XPS data (Fig. 3f) yielding a $Mn2p_{3/2}$ signal at 641.9 eV [38]. However, due to the closely spaced and highly convoluted nature of the Mn2p [38] and Fe2p [39] signals, no deconvolution attempts were on the Mn2p and Fe2p XPS data. Finally, $Fe2p_{3/2}$ XPS signal of MFS shown in Fig. 3g revealing a maximum at 712.1 eV and the corresponding Fe3s splitting value of 6.4 eV shown in Fig. 3e are consistent with the predominant existence of Fe^{3+} sites in MFS with a possible minor contribution from Fe^{4+} sites [40].

In overall, currently presented detailed XPS results indicate that the superior electrochemical performance of the 2D-MFS nanoplatelets can be ascribed to: *i)* the enrichment of polysulfide species on the MFS surface, *ii)* existence of a variety of $Mn^{2+/3+/4+}$, $Fe^{3+/4+}$ surface species providing redox versatility, *iii)* presence of unique $Fe_xMn_yO_zS_n$ surface domains, *iv)* smaller extent of surface sulfites, and *v)* a high Fe:Mn surface metal cation ratio of 0.7:0.3, as well as vi) a smaller extent of residual N and Cl atoms blocking the surface sites less than that of MnS. The MFS-CC samples were gently cleaned to avoid active material loss or CC damage. However, this process did not fully remove the residual N and Cl atoms. Consequently, MFS-CCs were used with these residues.

The electrochemical performance of the as-prepared electrodes was evaluated within three electrode setup using cyclic voltammetry (CV), galvanostatic charge-discharge (GCD), and potentiostatic impedance spectroscopy (PEIS) techniques. The electrolyte was 1.0 M potassium hydroxide (KOH(aq)), the reference electrode was saturated calomel electrode (SCE), and the counter electrode was platinum foil. Electrochemical characteristics of the MFS-CC in three-electrode configuration are provided in Fig. 4. The CV curves of the MFS-CC electrode in various sweep rates in a potential window of −1.0 V to −0.2 V are presented for comparison in Fig. 4a–b, respectively. Even at high scan rates, the performance of MFS-CC electrodes preserved its unique shape, showcasing its ability to work at high-rate applications. The appearance of two different discharge curves in the GCD measurements in Fig. 4c further

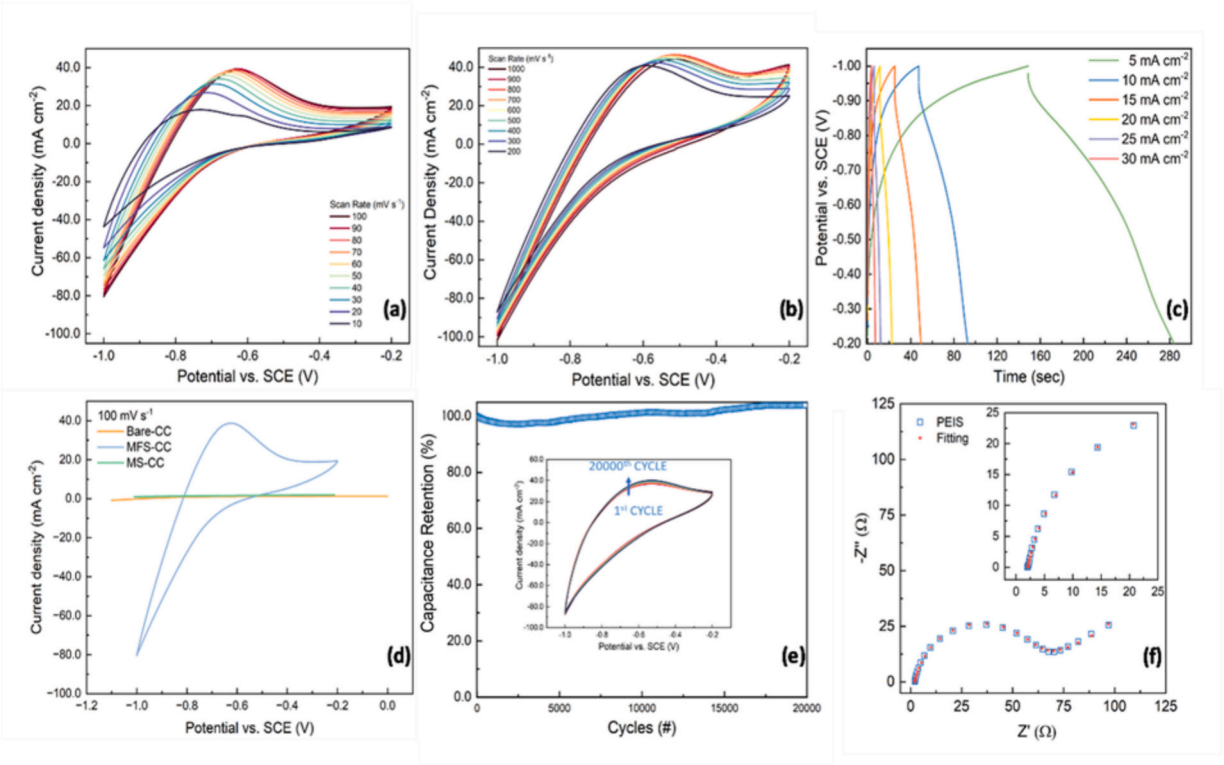

Fig. 4. Three electrode measurements (a) CV curves of MFS-CC electrode at low scan rates, (b) CV curves of MFS-CC electrode at high scan rates, (c) GCD curves of MFS-CC electrode, (d) CV curves of Bare-CC, MFS-CC, and MS-CC at a scan rate of 100 mV s^{-1}, (e) Cycling stability test for 20,000 cycles as shown by the capacitance retention plot with the corresponding CV profile from 1st cycle to 20000th cycle at the inset, (f) Nyquist plots of MFS-CC electrode with the inset showing enlarged high-frequency region.

supported the existence of pseudocapacitive redox reactions, consistent with those seen in the CV curves. The charging reactions of the MFSs are believed to be as follows;

$$4H_2O + 4e^- \leftrightarrow 2H_2 + 4OH^- \quad (1)$$

$$Fe_xMn_yO_zS_n + OH^- \leftrightarrow Fe_xMn_yO_zS_n(OH) + e^- \quad (2)$$

$$Fe_xMn_yO_zS_n + mK^+ + me^- \leftrightarrow K_mFe_xMn_yO_zS_n \quad (3)$$

A possible hydrogen evolution reaction (HER) generates hydroxide-rich surface on the MFS electrodes (see Eq. (1)). This hydroxide-rich surface might result in the conversion of the surface domains of MFS into $Fe_xMn_yO_zS_n(OH)$ (see Eq. (2)). Moreover, K^+ ions might be inserted into the MFS structure independently from the formation of hydroxide, causing the formation of $K_mFe_xMn_yO_zS_n$ species on the surface (see Eq. (3)) [41,42]. At a current density of 5 mA cm^{-2}, Coulombic efficiency was 91 %, which increased to 97 % at a current density of 30 mA cm^{-2}, indicating an excellent supercapacitive behavior. Gravimetric capacitance values with changing scan rates are provided in Fig. S7, and a corresponding decrease in the specific capacitance was observed with increasing scan rates, aligning with the expectations. The maximum specific capacitance attained for the fabricated MFS-CC electrode was 206 F g^{-1} and 232 mF cm^{-2} at a scan rate of 10 mV s^{-1}. The attained performance demonstrated a significant improvement in contrast to MS-CC, as clearly depicted in the comparative analysis shown in Fig. 4d. MS-CC did not show capacitive behavior (Figs. S8, S9), indicating the significance of stabilized pyrrhotite phase due to Mn doping. The stability of the MFS-CC electrodes was also investigated through CV measurement conducted for 20,000 cycles at a scan rate of 200 mV s^{-1}, results of which are provided in Fig. 4e. Capacitance retention initially decreased to 97 % followed by an increase to 103 % at the end of 20,000 cycles. The mechanism for the increase was elusive, as no drastic changes were observed in the CV graphs given in the inset in Fig. 4e. The enhancement might be due to improved pore accessibility during cycling and partial irreversible oxidation of the MFS. Since both the ionic and atomic radii of S are larger than those of O, this could reduce packing efficiency in the MFS lattice, potentially enhancing electrolyte access and contributing to improved performance. The PEIS measurements in Fig. 4f show a pseudocapacitive behavior with a wide semicircle in a wide frequency range with low impedance values. From the Bode impedance given in Fig. S10, the values of phase angle maxima were − 60° at a frequency of 20 Hz, and drastically increased to values close to 0° at other frequencies. This was also an indication of a pseudocapacitive behavior [43–45]. An electronic circuit model depending on the Nyquist curve and Bode plot was fitted and provided in Fig. S11. According to this model, two circuits containing constant phase element (CPE – Depicted with *Q*) was connected in parallel to Warburg impedance. The first CPE had a dimensionless exponent of 0.873, while the second had a modifier of 0.54. This further indicated a complex mechanism of double-layer capacitance and pseudocapacitance intertwined together, probably due to the 3D structure of CC and the nanoplatelet structure of MFSs. Firstly, the ultra-porous and nano-platelet structure of MFS-CC offered multiple electro-active sites (consistent with the presence of a variety of $Mn^{2+/3+/4+}$ and $Fe^{3+/4+}$ sites, surface enrichment with polysulfides, and $Fe_xMn_yO_zS_n$ surface species), facilitating redox reactions [46]. Secondly, the direct growth of MFS on the fiber established multiple 3D networks for adequate electron transportation during the charge transfer process [47].

A full-cell configuration (MFS-CC//AC-CC) was designed employing MFS-CC and AC-CC electrodes as the negative and positive electrodes, respectively. Comparisons between the MFS-CC and AC-CC in three-electrode configurations are provided in Fig. S12. At a scan rate of 200 mV s^{-1}, it is possible to see the enhanced energy storage of MFS-CC. MFS-CC//AC-CC asymmetric cells were prepared with a cellulose-based gel electrolyte for flexible and wearable device applications. Cellulose offers significant advantages when used to prepare gel electrolytes, mainly due to its superior water retention capabilities compared to widely used polyvinyl alcohol (PVA). Cellulose showcases exceptional hydrophilic properties, allowing it to effectively retain water within its gel-like structure [48]. This high water retention ability contributes to improved ionic conductivity and enhances the overall performance of the gel electrolyte [49]. Incorporating cellulose in gel electrolytes ensures prolonged moisture retention, providing a stable environment for ion transport and facilitating efficient electrochemical reactions [50]. Therefore, these advantages positioned cellulose as a prior gel-electrolyte choice to enhance the performance and longevity of the device. A non-woven disposable cloth as a separator was dipped into KOH-Hydroxyethyl-cellulose (HEC) gel electrolyte, then assembled with the MFS-CC and AC-CC to form a wearable supercapacitor cell. Photos and SEM images of the cloth are given in Fig. S13. These asymmetrical devices were formed and encapsulated with PVC layers using hydrophobic CC strips as the electrical contacts. Hydrophobic contacts prevented the discharge of the gel electrolyte via wetting. Fig. 5a-i and ii shows optical images of enclosed MFS-CC//AC-CC asymmetric wearable supercapacitor devices. Fig. 5a-iii illustrates the schematic assembly of the device. CV curves at various scan rates in the range of 0 V - 1.4 V can be seen in Fig. 5b. A maximum specific capacitance of 18.6 F g^{-1} and 42.4 mF cm^{-2} was obtained at a scan rate of 10 mV s^{-1}. The loss in specific capacitance was partially due to the gel electrolyte and the partial loss of performance due to the ineffective use of the 3D structure of the textile. While the redox peaks revealed the pseudocapacitive character of the fabricated device, CV curves from lower to higher scan rates exhibit similar profiles without severe distortion, indicating the device's excellent charge/discharge performance. Furthermore, the GCD test was carried out over a wide range of current densities (1–5 mA cm^{-2}) to clarify the electrochemical performance of the fabricated device. Resulting curves are provided in Fig. 5c. Particularly, at a current density of 1 mA cm^{-2}, two different charging slopes can be observed, which was attributed to the mechanism of MFS-CC. From the GCD curves, the specific energy density (*E*) and specific power density (*P*) of the device were also calculated. The maximum energy density and power density were found as 1.70 Wh kg^{-1} and 163 W kg^{-1}, respectively. A Ragone plot was drawn and provided in Fig. S14, showcasing the ideal performance of the MFS-CC//AC-CC wearable supercapacitor devices.

Fig. 5d shows the Nyquist plot of the wearable MFS-CC-based asymmetric supercapacitor device. The exceptional construction of the device was evidenced by the presence of minimal series resistance (~ 14 Ω) observed in the semicircular region at high frequencies, signifying optimal performance. This desirable characteristic was attributed to the use of hydrophobic CC contacts and the gel electrolyte based on HEC. A small semi-circle at high frequencies indicated an interfacial resistance originating from the thickness and conductivity of the gel electrolyte of the textile-based separator. Moreover, linear behavior with a 45° angle observed in the low-frequency region of the Nyquist plot indicated the occurrence of Warburg diffusion, aligning with the anticipated pseudocapacitive behavior observed in three-electrode measurements and facilitated by the employed gel electrolyte. The capability and the durability of the device were significantly enhanced through the implementation of the encapsulation strategy coupled with PVC lamination, showcasing an impressive total of 11,000 cycles as shown by the inset in Fig. 5e. More interestingly, device performance increased during the continuous usage of the cell. The initial specific capacitance at a scan rate of 200 mV s^{-1} was 5.8 F g^{-1}, which was improved to 8.4 F g^{-1} after the standard evaluation of the cell (including GCD and PEIS measurements) and improved to 11.5 F g^{-1} after 11,000 cycles. Relevant CV graphs are provided in Fig. 5f. The improvement was also seen in the three-electrode configuration, while the exact mechanism of this behavior is still not yet fully understood. We believe that the electro-activation process might cause the improvement in performance and long-term stability of MFS-CC//AC-CC upon increasing both the time and the number of cycles, which facilitates more soaking and activation of the 3D network of these materials with the gel electrolyte [51,52].

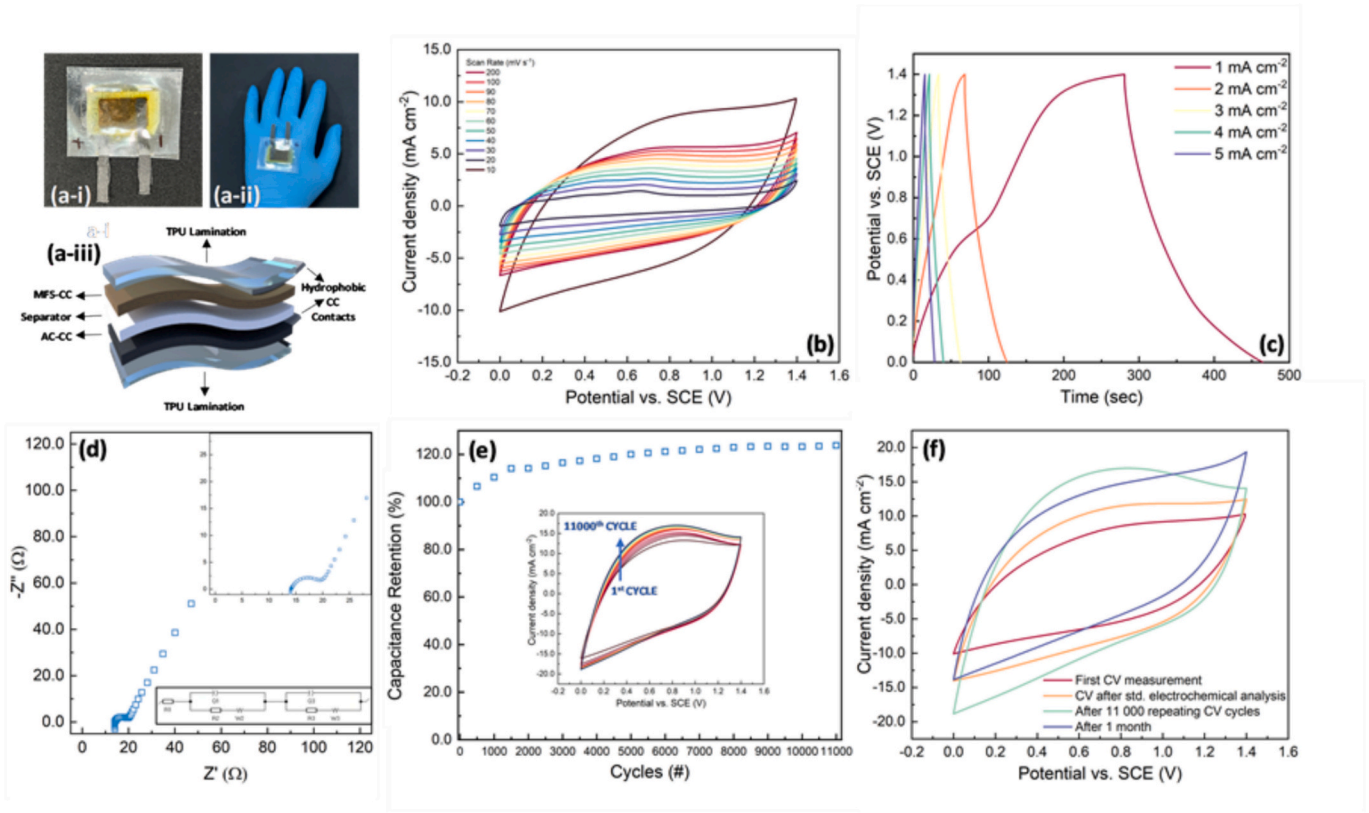

Fig. 5. Full-cell asymmetric device measurements (a) Configuration of the asymmetric wearable supercapacitor. (a-i, ii) Photos of the full-cell configuration. (a-iii) Schematic illustration of the flexible and wearable device. (b) CV profiles at various scan rates from 200 mV s^{-1} to 10 mV s^{-1}. (c) GCD curves at different current densities. (d) EIS data. The inset shows the enlarged high-frequency region and equivalent circuit model of the fabricated wearable and flexible device. (e) Capacitance retention plot at a scan rate of 200 mV s^{-1} for 11,000 cycles with the inset showing CV profiles from the 1st to 11000th cycle. (f) CV responses after operation and one month of storage.

The prepared wearable supercapacitor was also investigated after one month of storage to evaluate any potential effects on its performance. The capacitance value dropped to 8.8 F g^{-1}, which was still much higher than its initial state. Therefore, the unique strategy of PVC lamination on top of HEC-based electrolytes fulfilled the goal of long-term use. This makes MFS-CC-based wearable supercapacitors promising for future research and development for powering wearable electronics.

The viability of the self-powered wearable and flexible supercapacitor was further evaluated by connecting them in series and parallel configurations. Fig. 6a–b shows the CV and GCD profiles of the single, two, and three asymmetric devices connected in series. The output of two and three devices connected in series demonstrated a broader potential window up to 4.2 V, as compared to a single device operating at 1.4 V. Similarly, when two or three devices were connected in series, increasing the voltage shortened the charge-discharge times proportionally (10 mA cm^{-2}). Fig. 6c shows a photograph of a green light-emitting diode (LED) powered by the serially connected devices. With these three serially connected cells, a green LED (50 mA current at 2.8 V for maximum illumination) could be powered. Additionally, mixed serial and parallel connections were established, seamlessly scaling in accordance with the anticipated behavior (Fig. 6d–i). Four devices, assembled with a combination of series and parallel connections, were utilized to power the LED attached to a hoodie (Fig. 6d-ii and iii). These results verified that MFS-CC//AC-CC asymmetric wearable supercapacitors can be interconnected in series or parallel to power diverse wearable electronic devices.

The most important aspect of a wearable supercapacitor is its ability to be bent without performance loss. Fig. 6e-i shows the CV profile of the MFS-CC//AC-CC wearable device under various bending configurations at a scan rate of 200 mV s^{-1}. Relevant photographs are given in Fig. 6e-ii and e-iii. The MFS-CC//AC-CC asymmetric wearable supercapacitor device has demonstrated notable mechanical stability, as illustrated by the CV curves. This stability was evident across both rolled and folded configurations, showing remarkably identical behavior. The device's impressive flexibility and bendability characteristics were noteworthy, highlighting its potential utilization in wearable and flexible systems. Table S1 was tabulated to show that our work allows the fabrication of flexible and wearable supercapacitors by allowing the conformal coating of CC with Mn-stabilized FeS structure.

4. Conclusions

In conclusion, this study presents a promising method for the direct growth of manganese-doped iron sulfide nanoplatelets on carbon cloth fibers, creating homogeneously decorated MFS-CC electrodes. These electrodes exhibited remarkable electrochemical performances, delivering a maximum specific capacitance of 206 F g^{-1} and exceptional operation for 11,000 cycles. Moreover, encapsulating these electrodes guarantees their efficient operation for an extended period of one month. The successful construction of a self-powered, flexible, and wearable supercapacitor that lights up a green LED when placed onto a hoodie illustrates the remarkable potential of the device for real-world flexible and wearable applications. This work marks a significant step in energy storage, paving the way for the fabrication of high-performance, flexible, and wearable electronics.

CRediT authorship contribution statement

Almila Nur Gözütok: Writing – review & editing, Writing – original draft, Methodology, Investigation, Formal analysis, Data curation. **Mete**

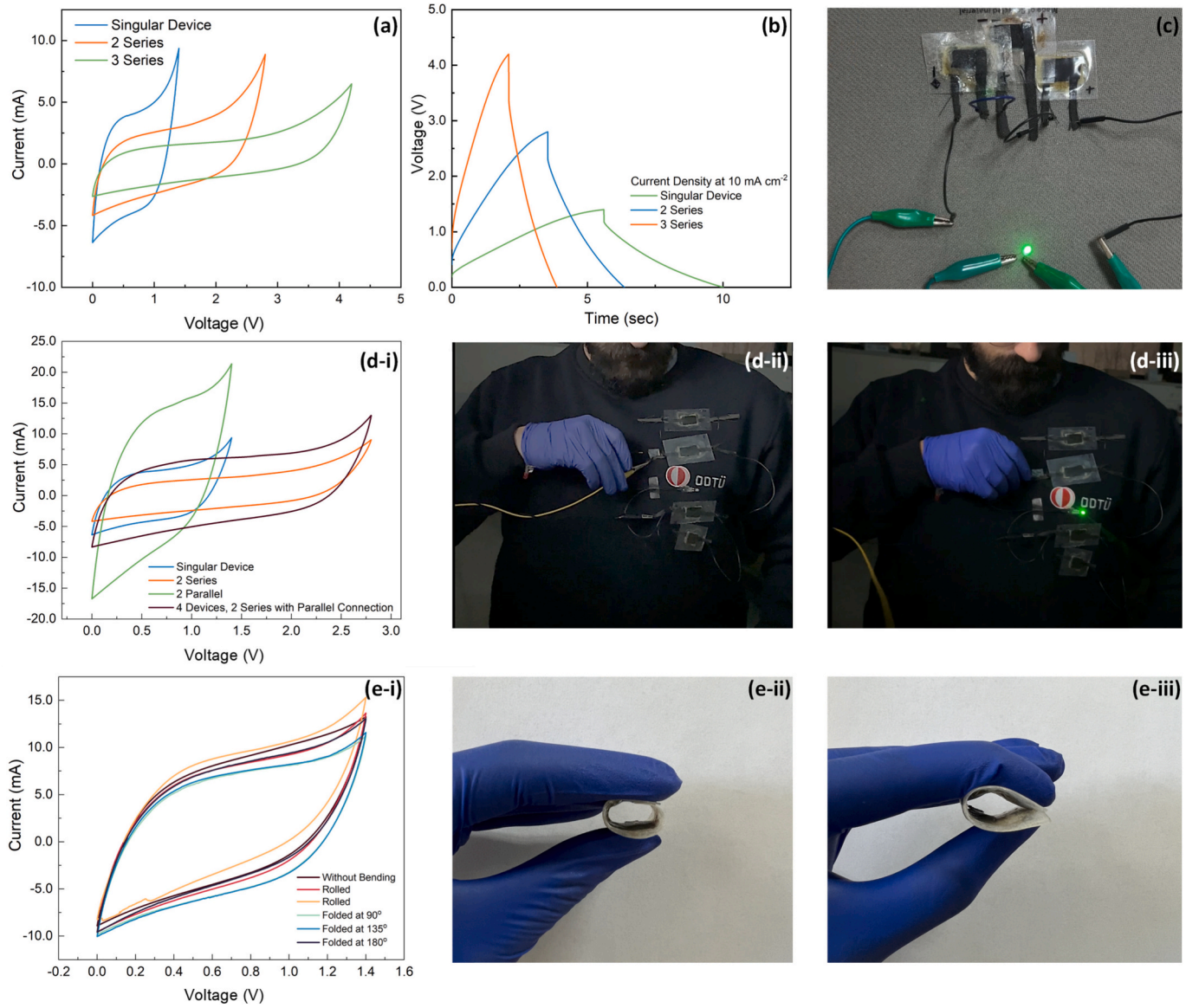

Fig. 6. Assembly of MFS-CC based asymmetric wearable and flexible supercapacitors in different configurations and resulting applications (a) CV (at a scan rate of 200 mV s^{-1}) and (b) GCD (at a current density of 10 mA cm^{-2}) measurements of wearable supercapacitor in different series configurations. (c) Photo of 3 serially connected supercapacitors lighting up a green LED (d-i) CV measurements of serial and parallel connections of the supercapacitors (d-ii, iii) Photos of green LED embedded in a hoodie with lights off and on. (e-i) CV measurements of the assembled device subjected to various bending applications. (e-ii, iii) Flexible and wearable device at two different bending scenarios. (For interpretation of the references to color in this figure legend, the reader is referred to the web version of this article.)

Batuhan Durukan: Writing – review & editing, Writing – original draft, Software, Resources, Methodology, Investigation, Formal analysis, Data curation, Conceptualization. **Yusuf Kocak:** Writing – review & editing, Writing – original draft, Methodology, Investigation, Formal analysis, Data curation. **Emrah Ozensoy:** Writing – review & editing, Writing – original draft, Methodology, Investigation, Formal analysis, Data curation. **Husnu Emrah Unalan:** Writing – review & editing, Writing – original draft, Supervision, Conceptualization. **Emren Nalbant:** Writing – review & editing, Writing – original draft, Supervision, Project administration, Funding acquisition, Conceptualization.

Declaration of competing interest

The authors declare the following financial interests/personal relationships which may be considered as potential competing interests: Emren Nalbant reports financial support was provided by Middle East Technical University. If there are other authors, they declare that they have no known competing financial interests or personal relationships that could have appeared to influence the work reported in this paper.

Acknowledgments

The authors wish to thank Ceren Şefaat for her assistance with the illustrations. This work was partially funded by the Middle East Technical University Scientific Research Projects Coordination Unit (BAPSIS) under the grant number TEZ-YL-103-2022-10906.

Appendix A. Supplementary data

Supplementary data to this article can be found online at https://doi.org/10.1016/j.est.2024.115182.

Data availability

Data will be made available on request.

References

[1] J. Wen, B. Xu, Y. Gao, M. Li, H. Fu, Wearable technologies enable high-performance textile supercapacitors with flexible, breathable and wearable characteristics for future energy storage, Energy Storage Materials 37 (2021) 94–122.

[2] M.R. Islam, S. Afroj, K.S. Novoselov, N. Karim, Smart electronic textile-based wearable supercapacitors, Adv. Sci. 9 (2022) 2203856.

[3] K. Jost, G. Dion, Y. Gogotsi, Textile energy storage in perspective, J. Mater. Chem. A 2 (2014) 10776.

[4] C.V.V. Muralee Gopi, R. Vinodh, S. Sambasivam, I.M. Obaidat, H.J. Kim, Recent progress of advanced energy storage materials for flexible and wearable supercapacitor: from design and development to applications, Journal of Energy Storage 27 (2020) 101035.

[5] D.P. Dubal, N.R. Chodankar, D.H. Kim, P. Gomez-Romero, Towards flexible solid-state supercapacitors for smart and wearable electronics, Chem. Soc. Rev. 47 (2018) 2065–2129.

[6] C. Liu, et al., Toward superior capacitive energy storage: recent advances in pore engineering for dense electrodes, Adv. Mater. 30 (2018) 1–14.

[7] G. Wang, L. Zhang, J. Zhang, A review of electrode materials for electrochemical supercapacitors, Chem. Soc. Rev. 41 (2012) 797–828.

[8] T. Wang, H.C. Chen, F. Yu, X.S. Zhao, H. Wang, Boosting the cycling stability of transition metal compounds-based supercapacitors, Energy Storage Materials 16 (2019) 545–573.

[9] Y. Gao, L. Zhao, Review on recent advances in nanostructured transition-metal-sulfide-based electrode materials for cathode materials of asymmetric supercapacitors, Chem. Eng. J. 430 (2022) 132745.

[10] Abdel Maksoud, M. I. A. et al. Advanced materials and technologies for supercapacitors used in energy conversion and storage: a review. Environmental Chemistry Letters vol. 19 (Springer International Publishing, 2021).

[11] L. Shen, et al., NiCo2S4 nanosheets grown on nitrogen-doped carbon foams as an advanced electrode for supercapacitors, Adv. Energy Mater. 5 (2015) 2–8.

[12] S.E. Moosavifard, S. Fani, M. Rahmanian, Hierarchical CuCo2S4 hollow nanoneedle arrays as novel binder-free electrodes for high-performance asymmetric supercapacitors, Chem. Commun. 52 (2016) 4517–4520.

[13] P. Rupa Ranjani, P.M. Anjana, R.B. Rakhi, Solvothermal synthesis of CuFeS2 nanoflakes as a promising electrode material for supercapacitors, Journal of Energy Storage 33 (2021) 102063.

[14] R. Liu, et al., Fundamentals, advances and challenges of transition metal compounds-based supercapacitors, Chem. Eng. J. 412 (2021) 128611.

[15] T.E. Balaji, H. Tanaya Das, T. Maiyalagan, Recent trends in bimetallic oxides and their composites as electrode materials for supercapacitor applications, ChemElectroChem 8 (2021) 1723–1746.

[16] S. Fleischmann, et al., Pseudocapacitance: from fundamental understanding to high power energy storage materials, Chem. Rev. 120 (2020) 6738–6782.

[17] Zheng, S. *et al.* Transition-metal (Fe, Co, Ni) based metal-organic frameworks for electrochemical energy storage. Adv. Energy Mater. 7, 1–27 (2017).

[18] G. Yu, X. Xie, L. Pan, Z. Bao, Y. Cui, Hybrid nanostructured materials for high-performance electrochemical capacitors, Nano Energy 2 (2013) 213–234.

[19] S. Aloqayli, et al., Nanostructured cobalt oxide and cobalt sulfide for flexible, high performance and durable supercapacitors, Energy Storage Materials 8 (2017) 68–76.

[20] J. Qin, et al., 2D mesoporous MnO2 nanosheets for high-energy asymmetric micro-supercapacitors in water-in-salt gel electrolyte, Energy Storage Materials 18 (2019) 397–404.

[21] K. Zheng, et al., Valence and surface modulated vanadium oxide nanowires as new high-energy and durable negative electrode for flexible asymmetric supercapacitors, Energy Storage Materials 22 (2019) 410–417.

[22] R. Li, S. Wang, Z. Huang, F. Lu, T. He, NiCo2S4@Co(OH)2 core-shell nanotube arrays in situ grown on Ni foam for high performances asymmetric supercapcitors, J. Power Sources 312 (2016) 156–164.

[23] H. Chen, et al., Highly conductive NiCo2S4 urchin-like nanostructures for high-rate pseudocapacitors, Nanoscale 5 (2013) 8879–8883.

[24] Y. Zhang, et al., Facile fabrication of flower-like CuCo2S4 on Ni foam for supercapacitor application, J. Mater. Sci. 52 (2017) 9531–9538.

[25] A.M. Elshahawy, et al., Controllable MnCo2S4 nanostructures for high performance hybrid supercapacitors, J. Mater. Chem. A 5 (2017) 7494–7506.

[26] N. Xiu, K. Zhao, S. Lin, Z. Xu, Hierarchical nanosheets-anchored-on-microsheets FeCo2S4 arrays as binder-free electrode for high-performance hybrid supercapacitor, J. Alloys Compd. 805 (2019) 33–40.

[27] Li, D., Zhang, L., Liang, J. & Li, L. Understanding the formation of a cubic Mn0.6Fe0.4S solid-solution anode and its high performance for rechargeable lithium-ion batteries. J. Alloys Compd. 915, 0–19 (2022).

[28] L. Argueta-Figueroa, et al., Hydrothermal synthesis of pyrrhotite (Fex-1S) nanoplates and their antibacterial, cytotoxic activity study, Prog. Nat. Sci.: Mater. Int. 28 (2018) 447–455.

[29] A. Mishra, N.P. Shetti, S. Basu, K. Raghava Reddy, T.M. Aminabhavi, Carbon cloth-based hybrid materials as flexible electrochemical supercapacitors, ChemElectroChem 6 (2019) 5771–5786.

[30] W. Zeng, et al., Fiber-based wearable electronics: a review of materials, fabrication, devices, and applications, Adv. Mater. 26 (2014) 5310–5336.

[31] D.P. Dubal, et al., Supercapacitors based on flexible substrates: an overview, Energ. Technol. 2 (2014) 325–341.

[32] Y. You, et al., Subzero-temperature cathode for a sodium-ion battery, Adv. Mater. 28 (2016) 7243–7248.

[33] H. Chen, et al., Mn-doped FeS with larger lattice spacing as advance anode for sodium ion half/full battery, Chem. Eng. J. 450 (2022) 137960.

[34] S.H. Overbury, D.R. Mullins, D.R. Huntley, Lj Kundakovic, Chemisorption and reaction of sulfur dioxide with oxidized and reduced ceria surfaces, J. Phys. Chem. B 103 (1999) 11308–11317.

[35] B.J. Lindberg, et al., Molecular spectroscopy by means of ESCA II. Sulfur compounds. Correlation of electron binding energy with structure, Phys. Scr. 1 (1970) 286–298.

[36] L. Zhao, et al., Novel sulfur-containing polymeric cathode material prepared via an inverse vulcanization method for advanced lithium–sulfur batteries, ACS Appl. Energy Mater. 5 (2022) 7617–7626.

[37] V.R. Galakhov, et al., Mn 3 s exchange splitting in mixed-valence manganites, Phys. Rev. B 65 (2002) 113102.

[38] M. Fujiwara, T. Matsushita, S. Ikeda, Evaluation of Mn3s X-ray photoelectron spectroscopy for characterization of manganese complexes, J. Electron Spectrosc. Relat. Phenom. 74 (1995) 201–206.

[39] H.W. Nesbitt, I.J. Muir, X-ray photoelectron spectroscopic study of a pristine pyrite surface reacted with water vapour and air, Geochim. Cosmochim. Acta 58 (1994) 4667–4679.

[40] R. Dedryvère, et al., X-ray photoelectron spectroscopy investigations of carbon-coated Li_x $FePO_4$ materials, Chem. Mater. 20 (2008) 7164–7170.

[41] J. Parayangattil Jyothibasu, et al., Iron sulfide microspheres supported on cellulose-carbon nanotube conductive flexible film as an electrode material for aqueous-based symmetric supercapacitors with high voltage. ACS, Omega 9 (2024) 26582–26595.

[42] K.K. Upadhyay, T. Nguyen, T.M. Silva, M.J. Carmezim, M.F. Montemor, Pseudocapacitive behaviour of FeSx grown on stainless steel up to 1.8 V in aqueous electrolyte, Journal of Energy Storage 26 (2019) 100949.

[43] J.S. Ko, et al., Differentiating double-layer, psuedocapacitance, and battery-like mechanisms by analyzing impedance measurements in three dimensions, ACS Appl. Mater. Interfaces 12 (2020) 14071–14078.

[44] A.Ch. Lazanas, M.I. Prodromidis, Electrochemical impedance spectroscopy-a tutorial, ACS Meas. Sci. Au 3 (2023) 162–193.

[45] A. Lasia, The origin of the constant phase element, J. Phys. Chem. Lett. 13 (2022) 580–589.

[46] M.S. Javed, et al., Flexible full-solid state supercapacitors based on zinc sulfide spheres growing on carbon textile with superior charge storage, J. Mater. Chem. A 4 (2016) 667–674.

[47] L. Shen, Q. Che, H. Li, X. Zhang, Mesoporous $NiCo_2O_4$ nanowire arrays grown on carbon textiles as binder-free flexible electrodes for energy storage, Adv. Funct. Mater. 24 (2014) 2630–2637.

[48] Z. Sun, et al., Overview of cellulose-based flexible materials for supercapacitors, J. Mater. Chem. A 9 (2021) 7278–7300.

[49] H. Dai, et al., Polymer gel electrolytes for flexible supercapacitors: recent progress, challenges, and perspectives, Energy Storage Materials 34 (2021) 320–355.

[50] H. Nasution, et al., Hydrogel and effects of crosslinking agent on cellulose-based hydrogels: a review, Gels 8 (2022) 568.

[51] X. Xia, et al., High-quality metal oxide core/shell nanowire arrays on conductive substrates for electrochemical energy storage, ACS Nano 6 (2012) 5531–5538.

[52] V.A. Agubra, L. Zuniga, D. Flores, J. Villareal, M. Alcoutlabi, Composite nanofibers as advanced materials for Li-ion, Li-O2 and Li-S batteries, Electrochim. Acta 192 (2016) 529–550.